Micro-mechanical failure model of a ferritic-bainitic steel : consequence and interests of a dual-phase polycrystalline model

Q. Shi[a,b], F. Latourte[a,*], G. Cailletaud[b]

a. EDF R&D, Les Renardières, 77818 Moret sur Loing Cedex, France

b. MINES ParisTech, Centre des Matériaux, PSL Research University, CNRS UMR 7633, 91003 Evry Cedex

* Corresponding author

Résumé

Une méthodologie de calcul du comportement plastique et de la rupture d'un acier de cuve de réacteur nucléaire à eau pressurisée est proposée dans ce travail. Une approche micromécanique est adoptée, basée sur des calculs d'homogénéisation en champs moyens ou sur des calculs d'agrégats obtenus par tesselation de Voronoi.

Une loi de comportement de plasticité cristalline à base physique est adoptée, permettant de modéliser le comportement du fer pur et de l'acier de cuve sur une large gamme de température.

Le modèle de rupture se base sur l'expression d'une contrainte de Griffith sur des carbures dont la distribution est formulée à partir de données expérimentales, la probabilité de rupture étant alors calculée par une méthode de Monte-Carlo.

Ce type d'approche permet de s'intéresser aux sites d'amorçage de la rupture, en lien avec les hétérogénéités microstructurales (par exemple les interfaces ferrite-bainite). Une comparaison est également présentée entre les fonctions de répartition de probabilité de rupture obtenues pour des agrégats monophasés et biphasés de même comportement plastique effectif.

Abstract

A calculation method for the plastic behaviour and for the failure of a nuclear reactor pressure vessel (RPV) steel is proposed in this work. A micro-mechanical approach is chosen, based on mean field homogenization calculations or on Voronoi aggregate calculations.

A physically based crystal plasticity law is used, allowing to model the behaviour of pure iron and of RPV steel over a wide range of temperature.

The failure model is based on a Griffith stress expression at carbides whose distribution is proposed from experimental data. The failure probability is then computed using a Monte-Carlo approach.

The proposed approach allows to investigate failure initiation sites, in relation with microstructural heterogeneities such as ferrite-bainite interfaces. A comparison is provided between failure probability cumulative distribution functions obtained for single-phase or dual-phase aggregates of same effective tensile response.

Mots clefs : Approche locale de la rupture, Rupture fragile, Micromécanique, Acier bainitique

Introduction

In the context of pressurized water nuclear reactor operation, the integrity of the reactor pressure vessel (RPV) has to be guaranteed during routine operation and when subjected to accidental loading conditions. For example, the loss of coolant accident is associated to a cold water injection that induces an increase of pressure together with a rapid decrease of temperature. In this context, several integrity assessments of the RPV steel have been proposed, as for example the Master Curve method [1, 2] that relies on fracture toughness data for irradiated and un-irradiated material. Because several microstructural changes during irradiation are key in understanding and predicting the plastic response and fracture properties modification with irradiation [3–6], European projects have been proposed to develop multi-scale modeling strategies for the RPV internals and the RPV steel with the objective of predicting the fracture toughness from microstructural initial composition, neutron flux and fluence, and other reference data [7, 8].

In the multi-scale modeling strategy, one key scale is the crystal plasticity whose different underlying physics, needs, implementations and applications have been reviewed in [9]. Crystal plasticity can be used to derive isotropic von Mises plasticity laws for the pressure vessel using homogenization procedures, based on the single-crystal tensile response obtained from discrete dislocation dynamics and lower scale simulations, predictive by nature. Recent advances in small-scale modelling of body-centered cubic (bcc) iron single crystals have been reported in [10–13].

On the fracture mechanics side, most of the recently developed multi-scale models have been inspired by the local approach of Beremin [14], in which the failure probability is obtained from a Weibull stress distribution identified from J2-plasticity finite element calculation results. In the case of polycrystalline aggregates, crystal plasticity is used to generate microstructural stress fields that are then compared with a local Griffith stress formulated by means of a surface energy, an average carbide density and a carbide size distribution function [15–17]. The latter results have been obtained by considering idealized Voronoi microstructures, and therefore the validity of a micromechanical failure approach should be questionned in view of the complexity of the bainitic microstructure [18] and of the relationships between microstructural modeling and calculated stress fields [19, 20].

In this context, the objective of this work is to introduce a novel RPV microstructural model taking advantage of recent physically based crystal plasticity constitutive equations, and to evaluate this model in term of brittle failure properties in the low temperature regime.

The paper is structured as follows. First, the RPV material is described. Then, a crystal plasticity model is tested for pure iron and identified for RPV steel according to two different modeling possibilities : single phase material or dual-phase material description. Finally,

	Mn	Ni	Mo	Si	C	Cr	Cu	Al	Co	P	S	V
Weight %	1.37	0.7	0.5	0.24	0.159	0.17	0.06	0.23	<0.01	0.005	0.008	<0.01

Table 1: Chemical composition of H1BQ12 material [21]

these two models are compared in term of failure probability results.

1 Material description

1.1 Large scale heterogeneities due to manufacturing

The RPV is a large scale component manufactured from forged ferrules of 280mm thickness made from low carbon steel 16MND5 (ASTM A508-3) whose chemical composition is provided in Table 1. This composition has been obtained for a reference material considered in this study, designed as H1BQ12 material and sampled from ferrule B's knockout H1 of the pressure vessel Q12. The pressure vessel height is 12.6m, and its diameter is 4.4m.

At room temperature, the thermodynamic equilibrium of 16MND5 steel provides a balance of pearlite and ferrite. In order to obtain a bainitic microstructure composed of bainite and ferrite, a heat treatment is applied following the 3-step recipe:

- Two austenitizations at a temperature between 865 °C and 895 °C followed by a water quench. Each austenization lasts 4 hours and 40 minutes.

- A 7.5 hours tempering at 630 °C- 645 °C

- A final annealing lasting 8 hours at a temperature of 610 °C

After this heat treatment, the steel exhibits a tempered bainitic microstructure. Starting from an austenite grain, ferrite laths grow from the grain boundaries during the cooling. Since carbon is much less soluble in ferrite than in austenite, it will start to diffuse from supersaturated ferrite to austenite. This enriched austenitic phase will then lead to the development of cementite at the interface between ferrite and austenite. The precipitation of carbides will therefore diminish the carbon concentration of austenite which will be able to transform into ferrite. If the cooling is slow enough, carbide precipitates will only precipitate at lath boundaries and in the end we will obtain upper bainite : the ferritic phase will be free from cementite. However, if the cooling is quick, some carbon atoms contained into supersaturated ferrite might not have the time to diffuse to the interface with austenite and will precipitate inside the ferrite laths leading to lower bainite. These phenomena are described in [22].

The tempering treatments are used to decompose the austenite that may remain between the laths of ferrite and to transform carbides into cementite. The tempering will decrease the steel hardness an in turn its brittleness. The annealing reduces remaining internal stresses.

In 16MND5 steel, pro-eutectoïd ferrite can nucleate at high temperature from prior austenitic grain boundaries for slow cooling conditions by diffusion processes. These equiaxed grains exhibit low carbon content (less than 0.02 wt.%) resulting in a very fine carbide precipitation.

Let us insist on the key microstructural average dimensions for 16MND5 steel. The austenitic grain size is 50 μm, the baintite lath is about 10 μm long and 1 μm thick, the size of the cementite precipitates at the grain boundaries is 1 μm in length and 0.2 μm in thickness and the cementite precipitates within the ferrite laths are spheric with a diameter of 0.1 μm[23]. Pro-eutectoïd ferrite grains are 10 μm in diameter.
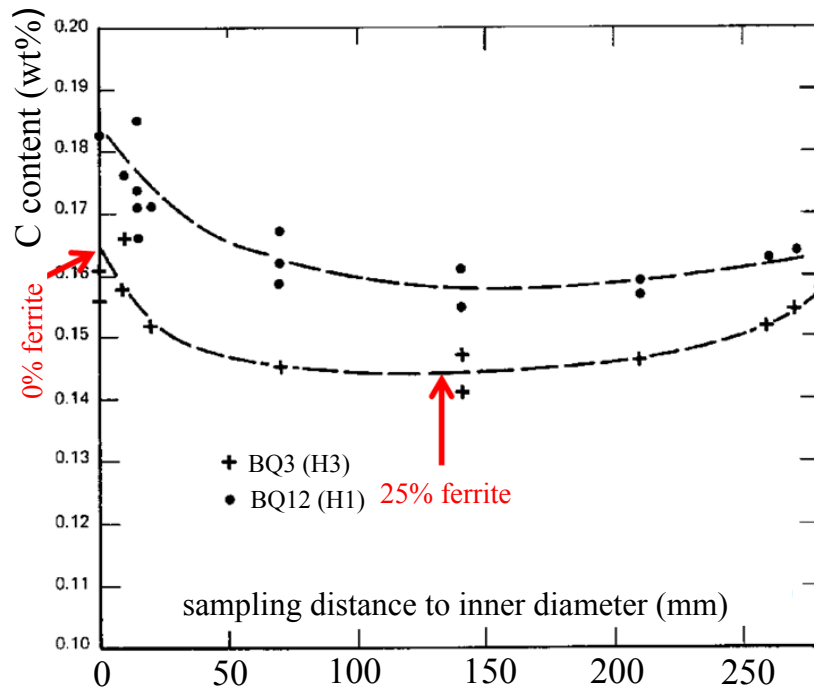

Figure 1: Carbon content in H1BQ12 steel versus the sampling position [24]
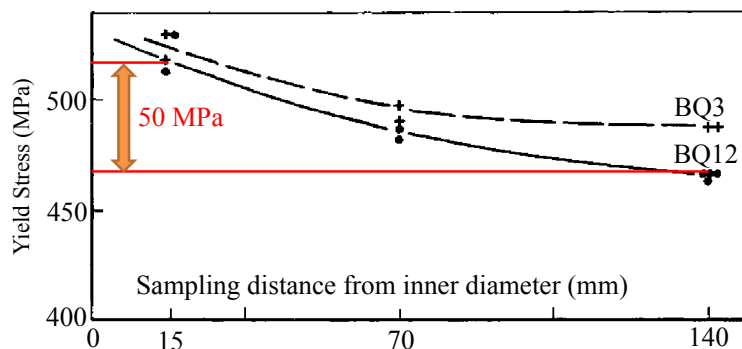

Figure 2: Yield stress of H1BQ12 steel versus the sampling position [24]

Given the production stages of 16MND5, and the sensitivity of the tempered bainitic microstructure to the process temperature and the cooling rate, the chemical composition, phase distribution and mechanical property are not uniform in the component thickness. As cooling rate is much slower in the core of the ferrule, more pro-eutectoid ferrite forms in this region, resulting in lower carbon content, lower tensile yield stress and strength. The variation in carbon content throught the thickness is shown in Figure 1 for two materials (H1BQ12
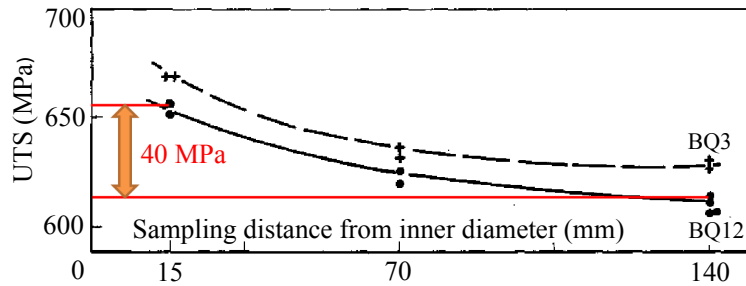
Figure 3: Ultimate tensile stress of H1BQ12 steel versus the sampling position [24]

Phase	1/2 depth $s_d = 140$mm	1/4 depth $s_d = 70$mm	inner diameter $s_d = 0 - 15$mm
Ferrite %	25 ± 3	16 ± 3	x
Carbide clusters %	25 ± 2	25 ± 1	15 ± 2
Bainite %	50	54	77
Martensite %	0	5 ± 4	18 ± 2

Table 2: Phase distribution at different sampling depths for H1BQ12 material [21]

and H3BQ3) obtained for two different pressure vessels. The variations of yield stress and ultimate tensile stress at room temperature are shown in Figures 2 and 3, respectively.

A large campaign of EBSD analyses on H3BC18 steel has allowed to characterize the fraction of phases present in the microstructure for three different sampling depths s_d : inner surface ($s_d \approx 0$ mm), quarter thickness ($s_d = 70$ mm) and half thickness ($s_d = 140$ mm) from the inner surface [21]. The main outcomes of this study has been summarized in Table 2.
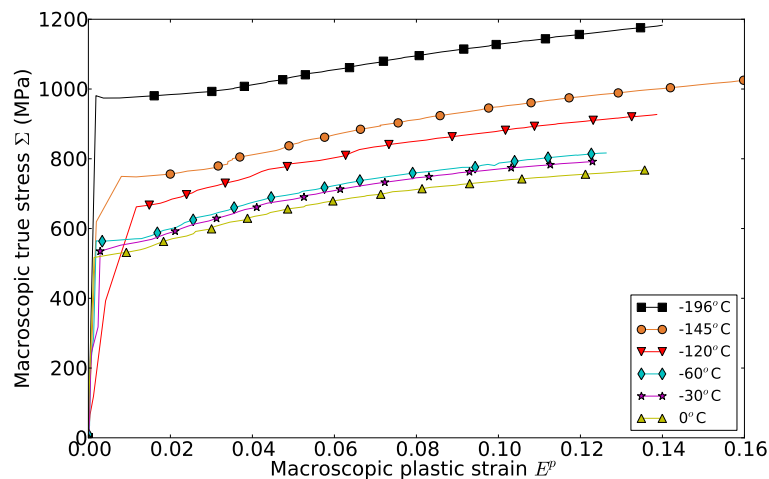
1.2 Tensile behavior

Figure 4: Stress-strain curves of 16MND5 samples of 3/4 depth, H1BQ12 material, reproduced from [25]

The chosen 16MND5 material, H1BQ12, has been used in the following to validate the simulations and identify the model parameters. This material has been used in several PhD works [25–28] and is therefore a good reference material candidate.

The H1BQ12 reference tensile specimens were taken at a depth of three quarters of the thickness ($s_d = 210$mm). The tensile experiments were carried out at a strain rate of $4 \times 10^{-4}s^{-1}$ at temperatures ranging from -196 °C to 0 °C. The experiments on this material have been summarized in [25], and the tensile curves are gathered in Figure 4. An increase of yield stress is observed when the temperature decreases, while the hardening is slightly decreasing.

2 plastic flow behaviour of pure iron

2.1 DD_CC constitutive law

The DD_CC (Dislocation Dynamics for body Centered Cubic crystals) relation is a law introduced in [12] and [13] which is based on physical properties of near pure iron through dislocation dynamics simulations, extending earlier physical models only considering a low temperature mechanism [29]. The dislocation density on each slip system, ρ_s is an essential internal variable of the DD_CC law. This law physically describes the plastic slip of the 12 {110} slip systems which are known as the most active among the 48 possible systems {110},{112},{123}. For each system the slip direction is noted m_s and the normal to the slip plane is n_s.

As usual, the single crystal law is written as a relationship between the applied shear stress τ_s on a system s and the slip γ_s, related to the local stress tensor $\boldsymbol{\sigma}$ and plastic strain tensor $\boldsymbol{\varepsilon}^p$ by the Schmid tensor (or orientation tensor) $\boldsymbol{\mu}$:

$$\tau_s = \boldsymbol{\sigma} : \boldsymbol{\mu}_s \ , \ \ \dot{\boldsymbol{\varepsilon}} = \Sigma\dot{\gamma}_s\boldsymbol{\mu}_s \ , \ \ \boldsymbol{\mu}_s = \frac{1}{2}\left(m_s \otimes n_s + n_s \otimes m_s\right) \tag{1}$$

The law has been implemented in the finite element code Code_Aster and aims at modeling two main deformation mechanisms at low and high temperature presented in the following.

2.1.1 Low temperature

At low temperature, a predominant screw dislocation network is observed, moving according to a double kink mechanism.

At low temperature the slip rate $\dot{\gamma}_{nuc}^s$ can be expressed as a function of the effective shear stress, the average length of screw dislocations l^s, the mobile dislocation density ρ_m^s, the absolute temperature T and the activation energy for double-kink nucleation under a given activation energy ΔG:

$$\dot{\gamma}_{nuc}^s = \rho_m^s bH \cdot l^s\left(\boldsymbol{\rho}, \tau_{eff}^s\right) \ \cdot \exp\left(\frac{-\Delta G\left(\tau_{eff}^s\right)}{kT}\right)\frac{\tau_s}{|\tau_s|} \tag{2}$$

where H is a constant frequency factor, b stands for the burgers vector magnitude and k is the Boltzmann constant. In the case of iron, direct analyses of experimental loading curves [30] provided the following expression that was found to cover the entire stress range observed

in the thermal regime:

$$\Delta G\left(\tau_{eff}^s\right) = \Delta G_0 \left(1 - \sqrt{\frac{\left\langle \tau_{eff}^s \right\rangle_+}{\tau_0}}\right) \tag{3}$$

where $\langle x \rangle_+ = \frac{1}{2}(|x| + x)$ stands for the positive part of x, and the index s relates to each slip system s.

2.1.2 High temperature

At high temperature the plastic deformation is associated to a drag mechanism that can be modeled by means of a Norton law:

$$\dot{\gamma}_{drag}^s = \dot{\gamma}_0 \left(\frac{|\tau_{app}^s|}{\tau_c^s}\right)^n \cdot \frac{\tau_{app}^s}{|\tau_{app}^s|} \tag{4}$$

where $\dot{\gamma}_0$ is a constant, τ_c^s is the critical shear stress and n is the viscous exponent.

2.1.3 General case

In the general case, there is a competition between the two regimes and the total slip can be expressed as an harmonic average of $\dot{\gamma}_{drag}^s$ and $\dot{\gamma}_{nuc}^s$, giving weight to the most limiting slip mechanism:

$$\frac{1}{\dot{\gamma}^s} = \frac{1}{\dot{\gamma}_{nuc}^s} + \frac{1}{\dot{\gamma}_{drag}^s} \tag{5}$$

To resolve the low temperature deformation given by equation (2) some additional relations define the screw segment length:

$$l_s = max(\lambda_s - 2\alpha_{AT}^s R^s; l_c) \ \text{ with } l_c = 500b\,(T/T_0) \tag{6}$$

$$(\lambda^s + D_{obs})^{-1} = min\left(\sqrt{\rho_f^s}\,;\,(D_{obs} + 2R^s)\rho_f^s\right) \ \text{ with } \rho_f^s = \sum_{j \neq s} \rho^j, \tag{7}$$

$$R^s = \frac{\lambda^s}{2\alpha_{AT}^s}; \ \alpha_{AT}^s = \sqrt{\sum_{j \neq s} a_{AT}^{sj} \frac{\rho^j}{\rho_f^s}}, \tag{8}$$

where l_c is the critical length of a screw dislocation, λ is the average distance between two obstacles, D_{obs} is the average obstacle diameter, a_{AT} is the interaction matrix at high temperature, ρ_f^s is the forest dislocation density which is used to take into account the irradiation defects and finally T_0 is a reference temperature: 300 K. The interaction matrix of the 12 considered <111>{110} slip systems has been obtained from dislocations dynamics calculations [31] and is reduced such that only two independent parameters are considered: $a_{AT_{coli}}$ for the collinear systems which interact strongly and $a_{AT_{\neq coli}}$ for the non-collinear systems of weaker interaction.

Another important variable to resolve the equation (2) is the effective shear stress given by:

$$\tau_{eff}^s = \left|\tau_{app}^s\right| - \tau_c^s, \text{ with } \tau_c^s = \sqrt{\tau_{LR}^s{}^2 + \tau_{LT}^s{}^2} + \tau_F \tag{9}$$

$$\tau_{LR}^s = \mu b \sqrt{a_{AT}^{ss}\rho^s}; \quad \tau_{LT}^s = max\left[0 \; ; \; \alpha_{AT}^s \mu b \left(\frac{1}{\lambda^s} - \frac{1}{2\alpha_{AT}^s R^s + l_c}\right)\right] \tag{10}$$

where τ_{app}^s is the applied shear stress, τ_c^s is the critical shear stress, τ_F is a term accounting for the network drag, τ_{LR}^s is a self hardening term and τ_{LT} is related to the line tension.

The dislocation density evolution depends on the dislocations mean free path and requires the average diameter of the bainitic grains and two multiplication parameters called K_{self} and K_f.

$$\dot{\rho}^s = \left[\frac{1}{D_{lath}} + \frac{\sqrt{a^{ss}\rho^s}}{K_{self}} + \frac{\alpha^s\lambda^s\rho_f^s}{K_f} - y^s\rho^s\right]\frac{\dot{\gamma}^s}{b} \tag{11}$$

$$a^{sj} = a_{AT}^{sj}\left(1 - \frac{\tau_{eff}^s}{\tau_0}\right)^2 ; \quad \frac{1}{y^s} = \frac{1}{y_{AT}} + \frac{2\pi\tau_{eff}^s}{\mu b} \tag{12}$$

K_{self} and K_f are related to each other by the following equation:

$$K_f = \frac{K_{self}}{\beta} , \quad \beta = \min\left(3 \; ; \; 1 + \frac{2 \cdot T}{T_0}\right) \tag{13}$$

2.2 Tensile behaviour calculation technique

This model requires 15 different parameters but most of them can be determined using physical measurements like the average obstacle length, initial dislocation density, average lath dimension. Table 3 presents the values of these parameters identified in [13] on pure iron at temperatures ranging from -196 °C to 0 °C.

b (nm)	H (s^{-1})	ΔG_0 (eV)	τ_0 (MPa)	ρ_m (mm^{-2})	ρ_{ini} (mm^{-2})	$\dot{\gamma}_0$ (s^{-1})	n
0.248	$1 \cdot 10^{11}$	0.84	363	10^6	$7.2 \cdot 10^6$	10^{-6}	50

D_{obs} (nm)	y_{AT} (nm)	τ_F (MPa)	D_{lath} (mm)	$(a_{AT}^{sj})_{coli}$	$(a_{AT}^{sj})_{\neq coli}$	K_{self}
10	2	0	0.01	0.7	0.1	100

Table 3: Parameters used in DD_CC law for pure iron [13]

With the reference parameters, the strain-stress curve has been calculated first using a self-consistent Berveiller-Zaoui homogenization technique [32] and compared with experimental results.

When considering a self consistent model, each grain of the polycrystal is successively regarded as an inclusion within the matrix of the homogeneous equivalent medium (HEM). Each grain interacts therefore with the equivalent medium of the whole volume considered. The Berveiller-Zaoui rule assumes that elasticity is uniform and isotropic, that the grains are spherical and that the loading is monotonic. The localization equation writes:

$$\boldsymbol{\sigma}_g = \boldsymbol{\Sigma} + 2\alpha\mu\left(1 - \beta\right)\left(\boldsymbol{E}^p - \boldsymbol{\varepsilon}_g^p\right), \tag{14}$$

where g is a given grain, $\boldsymbol{\sigma}_g$ is the average stress tensor on g, $\boldsymbol{\Sigma}$ is the macroscopic stress tensor, μ is the elastic shear modulus, α is a parameter that can be approximated by equation (15), β is a parameter described in Kröner's model [33] and given by equation (17), $\boldsymbol{E}^p$ is the macroscopic plastic strain and $\boldsymbol{\varepsilon}_g^p$ is the average plastic strain on g.

$$\alpha^{-1} \approx 1 + \frac{3}{2}\mu E^p \Sigma^{-1}, \quad \text{with:} \tag{15}$$

$$(E^p)^2 = \frac{3}{2}\boldsymbol{E}^p : \boldsymbol{E}^p, \quad \Sigma^2 = \frac{3}{2}\boldsymbol{S} : \boldsymbol{S}, \quad \boldsymbol{S} = \boldsymbol{\Sigma} - \frac{1}{3}\mathrm{Tr}(\boldsymbol{\Sigma}) \tag{16}$$

$$\beta = \frac{2\left(4 - 5\nu\right)}{15\left(1 - \nu\right)} \approx 0.5 \text{ for } \nu = 0.3 \tag{17}$$

From the approximation in equation (17), equation (14) now writes:

$$\boldsymbol{\sigma}_g = \boldsymbol{\Sigma} + \alpha\mu\left(\boldsymbol{E}^p - \boldsymbol{\varepsilon}_g^p\right), \tag{18}$$

with the following homogenization rule:

$$\boldsymbol{E}^p = \sum_g x_g \dot{\varepsilon}_g^p, \tag{19}$$

where x_g is the volumetric fraction of grain g. The equations (18) and (19) are the equations solved by Code_Aster that was used to calculate the homogenized tensile response. An aggregate of 100 grains, of equal volume, and giving an isotropic texture, was considered.

For pure iron, the complete tensile curve is only available at room temperature and a good agreement is observed, except for the very early hardening stage ($\varepsilon < 0.015$) since the DD_CC law does not yet physically describe the complex transition from elastic elastic regime to microplasticity and plasticity. By sake of synthesis, this tensile response is not reported here. Some validations also not reported herein consisted in comparing the tensile behaviour obtained by homogenization with the one obtained by a finite element calculation of a 98 grain Voronoi polycrystal as already developed in [34], and the gap was found to be less than 5 MPa for 3% of macroscopic strain, for various orientation samplings and various tensile directions applied to the homogenized model.

In the following, the homogenized model response will be plotted against the experimental tensile yield stress from -196 °C to 0 °C.

2.3 Parameter sensitivity study

The following sensitivity study has been conducted for the main adjustable parameters. The parameters were modified one by one, leaving the other parameters fixed. This procedure allows to identify the mechanical role of each parameters and to provide some complementary validation of the reference value since the same experimental data as used in the original identification [13], obtained from [35] is shown in the cross plots.

Because the conventional yield stress $\sigma_{Y0.2}$ is obtained during the early stage of deformation, not well captured by the model, the sensitivity analysis is conducted by considering
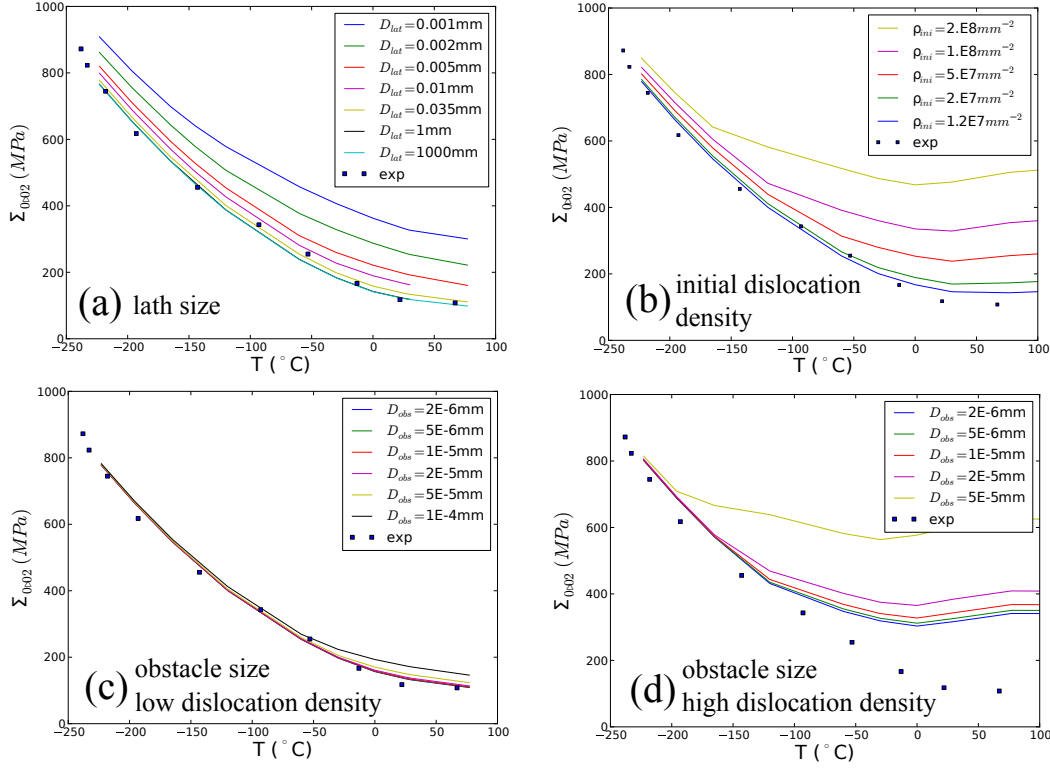
Figure 5: Yield stress sensitivity analysis results for some key model parameters

the macroscopic stress at 2% macroscopic plastic strain $\Sigma_{0.02}$. The result of the sensitivity analyses for the parameters influent on the yield stress are summarized in Figure 2.3.

From the results gathered in Figure 2.3, the following conclusions can be drawn:

- Figure 2.3a show that reducing the lath size D_{lat} significantly increases the yield stress $\Sigma_{0.02}$. This increase is rather uniform over the temperature range,

- Figure 2.3b show that increasing the dislocation density ρ_{ini} significantly increases the yield stress, more specifically in the high temperature regime ($T > -100\,°C$). The highest dislocation densities correspond to a work hardened material.

- Figure 2.3c and 2.3d show the effect of average obstacle size D_{obs} for low and high initial dislocation density respectively. The low value of ρ_{ini} is $7.2 \cdot 10^6 \mathrm{mm}^{-2}$, and the high value is $10^8 \mathrm{mm}^{-2}$. While no effect is obtained for low initial dislocation density, a strong yield stress increase is observed for high initial dislocation density. As in Figure 2.3b this effect is more pronounced in the high temperature regime.

From the results of Figure 2.3, the yield stress increase as a function of the lath size as been plotted at room temperature against the square root inverse of D_{lat}. For values above 5 (*i.e.* for $D_{lat} < 5\mu$m) the evolution is linear as shown by the green solid fitting line. This fit corresponds to the following Hall-Petch relationship:

$$\sigma_Y = \sigma_0 + A \cdot D_{lat}^{-1/2}, \ \ \sigma_0 = 85.4 \text{ MPa}, \ A = 0.25 \mathrm{MPa} \cdot \mathrm{m}^{1/2} \tag{20}$$
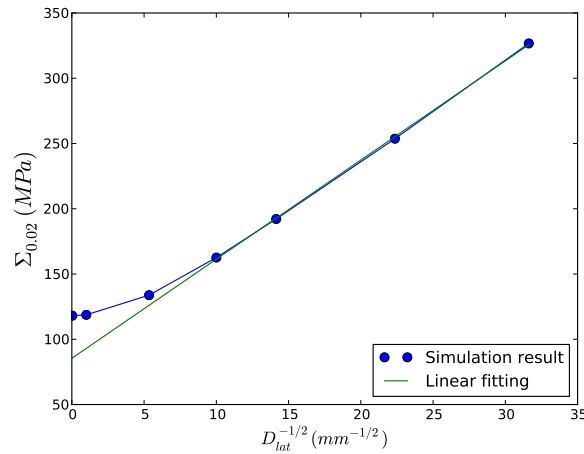
Figure 6: Linear fitting of $\Sigma_{0.02}$ over D_{lat}

In addition, the obtained slope A lies between the experimentally obtained values for interstitial free steel (0.14MPa · m$^{1/2}$) and 0.03wt% carbon steel (0.81MPa · m$^{1/2}$) [36].

Equation 11 is showing that K_{self} is influent on the dislocation multiplication rate. This is confirmed by figure 7(b) showing the effect of K_{self} on the hardening of pure iron, presented by the difference between $\Sigma_{0.1}$ and $\Sigma_{0.02}$. Decreasing K_{self} increases the hardening. As shown by Figure 7(a), K_{self} has a negligible influence on yield stress Both Figures 7(a) and 7(b) prove the validity of the reference value of $K_{self} = 100$ for pure iron.
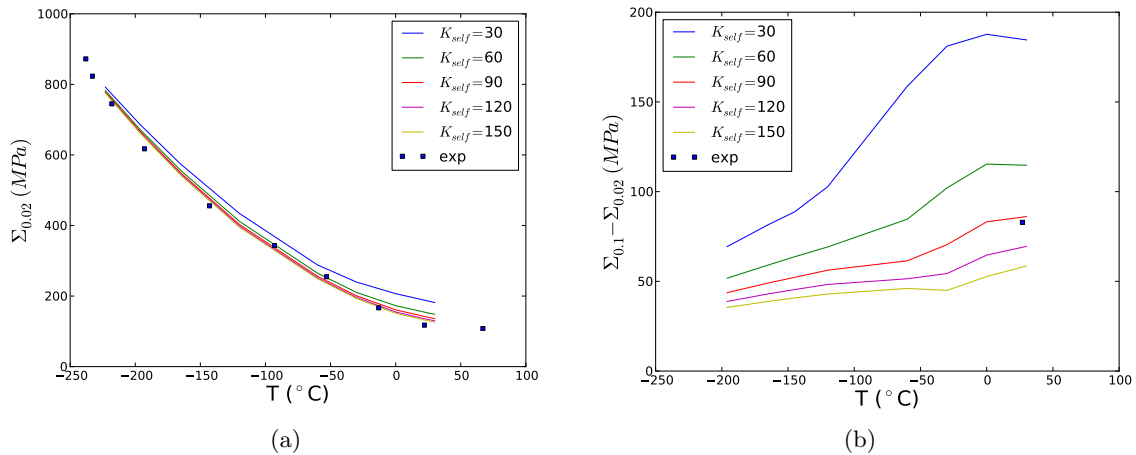

(a)

(b)

Figure 7: Influence of parameter K_{self}.

2.4 Adaptation to more complex materials

The model has been validated for the so called pure iron, which is a large grain polycristalline material with low carbon content. To now adapt the model to a more complex material of bainitic microstructure and of higher carbon content, therefore of higher yield stress, the principle is as follows:

- increase the dislocation density ρ_{ini} and eventually provide measured values for 16MND5. Note that this density is sensitive to the manufacturing (hot/cold work, heat treatment) and that measures rely on transmission electron microscopy analyses on thin foils and therefore are difficult to achieve and need to be repeated enough to be statistically representative,

- increase the obstacle size D_{obs} to the maximal obstacle size present in the microstructure, obstacles being carbides and dislocation junctions,

- decrease the lath size D_{lat} to the minimal mean free path for dislocations, *e.g.* grain dimension or lath thickness.

- eventually increase the alloy friction parameter τ_F to integrate both the solid solution hardening and the precipitation strengthening.

Starting from these general principles, the work conducted on 16MND5 material will be discussed in the following.

3   plastic flow behaviour of RPV steel

A specific strategy has been introduced in this work to model the RPV steel. The final objective of this work being to use polycrystalline stress fields to compute a failure criterion, an accurate micro-structural description is desired. As already introduced, depending on the sampling depth several phases coexist, the softer being pro-eutectoid ferrite, varying in volume proportion from 0% to 25%. It is then chosen to model the RPV steel as a dual phase model composed by ferrite (soft) and bainite (hard). To start with a simple model, the carbide clusters and martensite are considered as similar to the bainite.

   Using this approach, varying the ferrite proportion for example allows to capture the variations in yield stress and tensile strength with the sampling depth as reported experimentally in Figures 2 and 3.

   To illustrate this model, a realization example is shown in Figure 3. A 162 grain aggregate was generated first by a Voronoi tesselation and meshed using the open source Salome software embedding Netgen meshing procedure. A phase label is then attributed to the different grains to reach the desired ferrite fraction, by randomly picking ferrite grains. The ferrite fraction for this work has been set at 25%, representative of the ferrule half thickness.

   In the following, a smaller aggregate of 98 grains was used for the finite element calculations. Some informations on this mesh are provided in table 4. For the tensile loadings of this aggregate, the boundary conditions are imposed as average displacement conditions on the upper and lower faces (without planar condition) and the four lateral faces are let totally traction free.

	Volume	N(elements)	N(grains)
Whole model	100%	26718	98
Ferrite	24.96%	7092 (26.5%)	24
Bainite	75.04%	19626 (73.5%)	74

Table 4: Basic information for dual-phase Voronoï model with 75% bainite

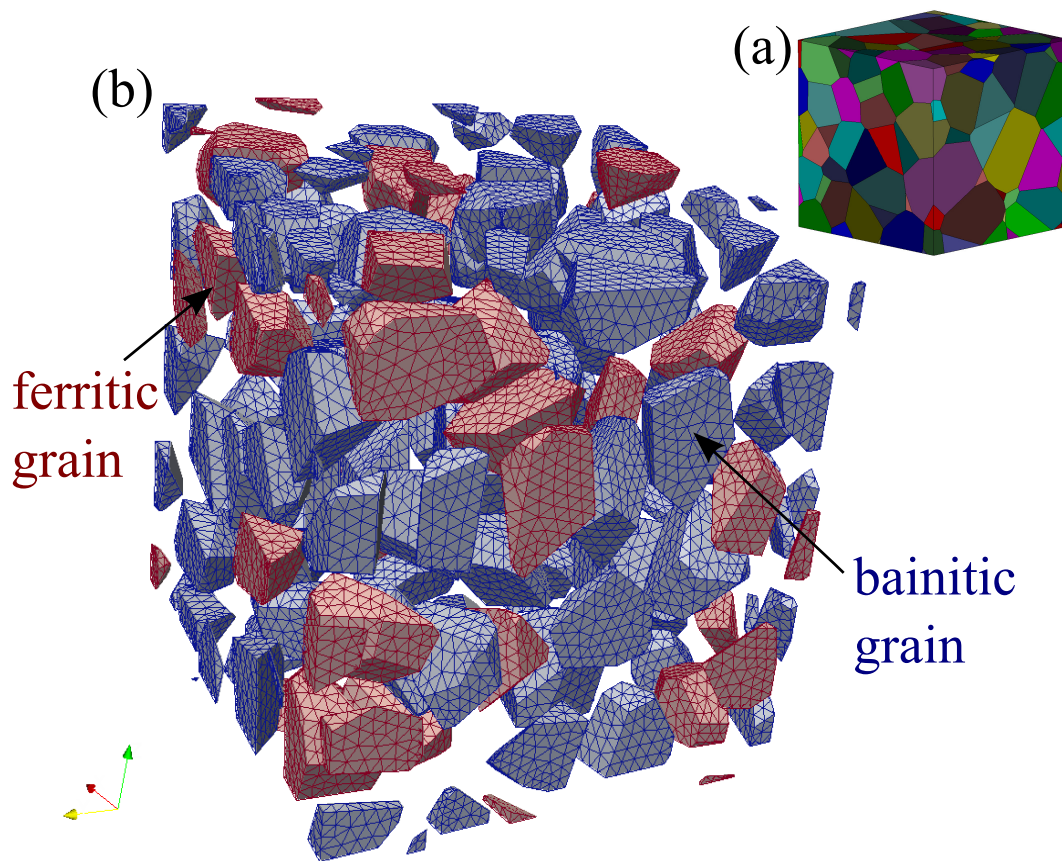Figure 8: Realization example of a 162 grain polycrystal, Voronoi tesselation (a) and exploded mesh showing the distribution of phases with 75% bainite content (b)

b (nm)	H (s^{-1})	ΔG_0 (eV)	τ_0 (MPa)	ρ_m (mm^{-2})	$\dot{\gamma}_0$ (s^{-1})	n	y_{AT} (nm)
0.248	$1 \cdot 10^{11}$	0.84	363	$1.2 \cdot 10^7$	10^{-6}	20	2
Phase	D_{obs} (nm)	ρ_{ini} (mm^{-2})	τ_F (MPa)	D_{lath} (mm)	$(a_{AT}^{sj})_{coli}$	$(a_{AT}^{sj})_{\neq coli}$	K_{self}
Ferrite	10	$2.4 \cdot 10^7$	8	0.088	0.7	0.1	30
Bainite	20	$1.3 \cdot 10^8$	85.4	0.005	0.7	0.1	30

Table 5: Parameters at -150 °C used in DD_CC law for dual-phase model

A list of parameters specific to each phase was identified by conducting tensile simulation on a dual-phase aggregate and optimizing the parameters by a Levenberg-Marquardt algorithm. Several parameters introduce the mechanical properties contrast between the two phases: the initial dislocation density, the alloy friction, the average lath size, the obstacle size, while the other parameters are kept identical (see Table 5).

b (nm)	H (s^{-1})	ΔG_0 (eV)	τ_0 (MPa)	ρ_m (mm^{-2})	$\dot{\gamma}_0$ (s^{-1})	n	y_{AT} (nm)
0.248	$1 \cdot 10^{11}$	0.84	363	$1.2 \cdot 10^7$	10^{-6}	20	2
D_{obs} (nm)	ρ_{ini} (mm^{-2})	τ_F (MPa)	D_{lath} (mm)	$(a_{AT}^{sj})_{coli}$	$(a_{AT}^{sj})_{\neq coli}$	K_{self}	
13	$1.08 \cdot 10^8$	60	0.005	0.7	0.1	30	

Table 6: Parameters at -150 °C used in DD_CC law for single-phase model

A second optimization was conducted by considering the material as single-phase. Although less physically detailed, this optimization provide a reference material of same effective response in tension, allowing to compare stress field heterogeneities between the two models without changing the average mechanical response. This second list of parameters is provided in Table 6.

Figure 9 demonstrates the good agreement between the two models, single-phase and dual-phase, with the experimental tensile data at -150 °C, a relevant temperature to conduct the fracture study. The voronoi aggregate mesh used to compute the tensile curves are also shown on the same Figure. Average stress-strain curves per grain in the tensile direction are reported Figure 10 and show that stresses in bainitic grains are higher than in ferritic grains, as expected, with a large scatter in stress levels as soon as yielding occurs. At 10% macroscopic strain, the average deformation of ferritic phase is 11% higher than that of bainite.

4 failure behaviour of RPV steel

At low temperature a possibility of brittle failure by cleavage exists for 16MND5 steel [37, 38]. Modeling the brittle failure is of industrial relevance and being able to predict its probability for irradiated material has been a key objective of European projects like Perfect and then Perform60 [7, 8]

Energy absorbed during fracture for 16MND5 steel shows that the ductile to brittle transition takes place between -150 °C and 0 °C [39]. Using the same single-phase and dual-phase 98 grain aggregate as introduced earlier to study the behaviour, additional crystal plasticity
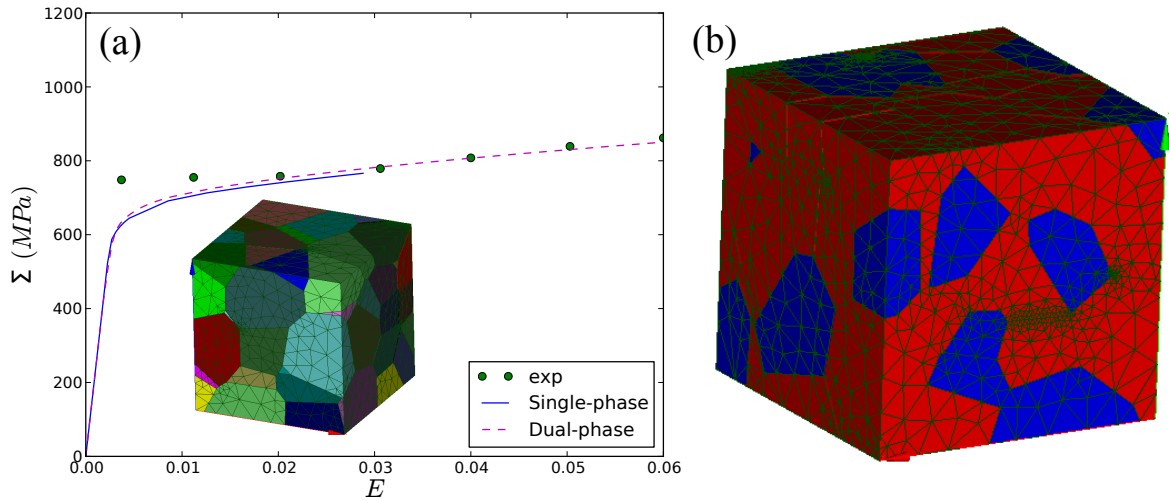
Figure 9: Macroscopic stress-strain curves at -150 °C compared with experimental values (a). The meshed aggregate used to compute the tensile curves is shown with colored grains (a) and colored phases for the 75% bainite fraction case (b).
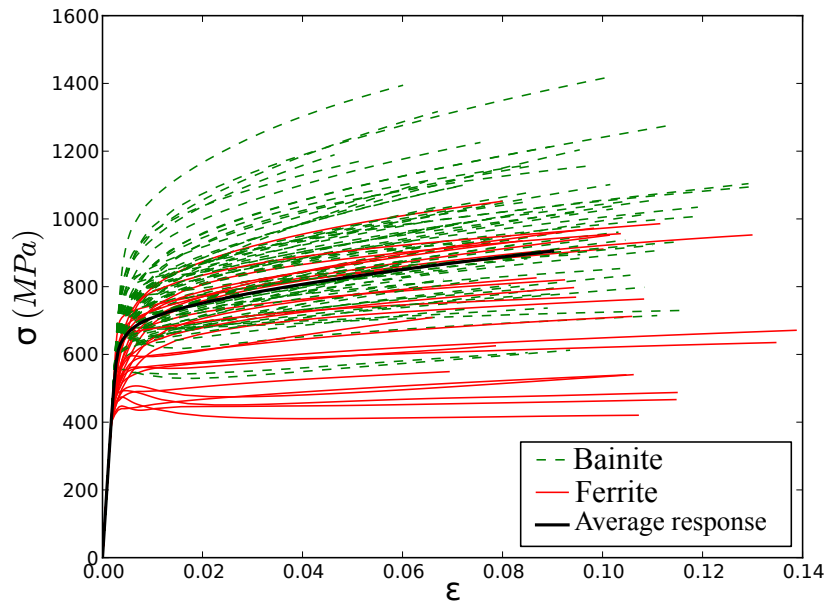

Figure 10: stress-strain curves for each grain for a model with 75% bainite with parameters of table 5

calculations were conducted at -196 °C and -150 °C since these two temperatures belong to the brittle failure domain. Loading conditions were triaxial with a chosen triaxiality of 2.5 (*cf.* Eq. 21) to represent the average stress field in front of a compact tension specimen crack tip. Practically, the loading was prescribed by imposing average loads to the 3 sets of adjacent faces by means of discrete linking elements and integral relationships, using the following relationship between average reactions in each direction:

$$\alpha\Sigma_1 = \Sigma_2 = \Sigma_3 \ , \ \alpha < 1 \ , \ \ \chi = \frac{1 + 2\alpha}{3 - 3\alpha} \tag{21}$$

The triaxiality was also computed after the calculation by averaging the triaxiality directly computed from the principal stresses, which validated the loading conditions. Since the conditions are imposed as average conditions, displacement fluctuations are allowed on each face and artificial stress concentrations are prevented. It is then possible to use a reasonably small representative volume as the elements near the boundary can be included in the post treated volume. The volume of the aggregate is set to $(50\mu m)^3$.

As shown by Figure 11, the macroscopic stresses in the three principal directions slightly differ between the single-phase and the dual phase calculations, while no mismatch was found in uniaxial tension. This difference can be attributed to the increased stress heterogeneities induced by dual-phase model and more pronounced for triaxial loadings, resulting in lower yield stress compared to the single phase model.
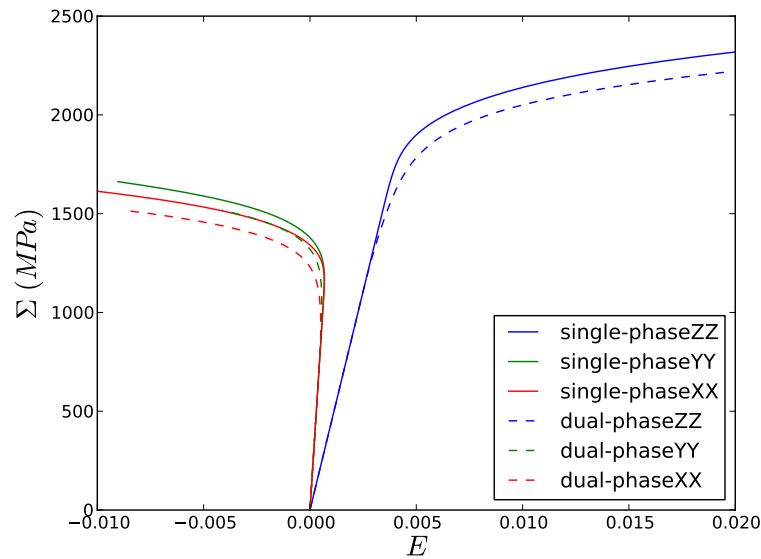

Figure 11: Average stress-strain curves in the three tensile components obtained during the triaxial tensile calculation at -150 °C.

4.1   Chosen local approach to failure model

The model used to predict failure is based on an earlier work in which a Beremin-type post treatment [14] was applied to the stress and strain fields computed for a polycrystalline aggregate [27]. This failure model is based on the following 6 hypotheses:

- **H1:** The carbides and other second phase particles are the initiating locations of fracture. The effect of larger particles (MnS) is not taken into consideration, since they mostly affect the ductile failure properties[39].

- **H2:** The plasticity is considered as mandatory (together with a critical stress) in the

initiation process. This will lead to consider a threshold of plastic deformation in the initiation criterion.

- **H3:** The carbide population is composed of clusters in the middle of bainitic laths and of larger isolated carbides. All these carbides are potential candidates to provoke cleavage. The defect sizes follow a Frechet distribution [40].

- **H4:** Once a crack initiates at a defect, its propagation in the neighbouring ferritic matrix is considered to be driven by a Griffith-style criterion. The ferrite cleavage principally takes place in the {001} family. The corresponding Griffith stress is given by:

$$\sigma_{Grif} = \sqrt{\frac{\pi E \gamma_p}{2(1 - \nu^2)a}}, \tag{22}$$

where E corresponds to Young's modulus, a is the crack size and γ_p, surface energy in J/m^2 term, is derived from a former optimization for 16MND5 [27]:

$$\gamma_p = 2.15 + 1.53 \cdot e^{0.009 \cdot T} \tag{23}$$

- **H5:** The largest defects (of dimension greater than r_c^{max}) are initiated in the beginning of plasticity deformation and are blunted instead of being propagated. As a result, there exists a threshold in carbide size, beyond which the cleavage mechanism will not be activated. In the following this threshold is set to one micron.

- **H6:** The overcome of micro-structural barriers is not a critical mechanism, as long as the stress needed for the propagation of a defect is reached. The weakest chain hypothesis is applied here : the propagation of a micro-defect in the ferritic matrix leads to the fracture of the considered volume.

A key data to apply such micromechanical failure model is about the carbide distribution in material. The study of steel Euro Material A by Ortner et al. [40] not only gives the size distribution of carbides, but also the carbide number per volume unit N:

$$p(r \geq r_0) = f(r_0) = 1 - exp(-(\frac{r_0}{3.6 \cdot 10^{-8}})^{-2.7}), N = (7.6 + 2.4) \cdot 10^{17} m^{-3} \tag{24}$$

$$n_{ave} = Nv, \sigma_0 = \sqrt{\frac{Nv}{2 \cdot 10^{11}}} \tag{25}$$

A given carbide number obtained from a truncated normal distribution of average n_{ave} and standard variation σ_0 [41] is distributed to each gauss point associated to an elementary the volume v. In this manner some gauss points do not get carbides, as shown in Figure 13(a), and some others get multiple carbides. In the latter case only the largest carbide is kept for the calculation of critical stress σ_{Grif}. Those gauss points without carbides are allocated with very high σ_{Grif}. By this method a distribution of critical cleavage stress is obtained, that is a function of r_c^{max} and γ_p.

Most local approaches calculate the critical stress based on the first principal stress but another stress measure is chosen in this model. As the crystal orientation for each gauss point is known, the projection of stress tensor on the cleavage planes can be easily performed,
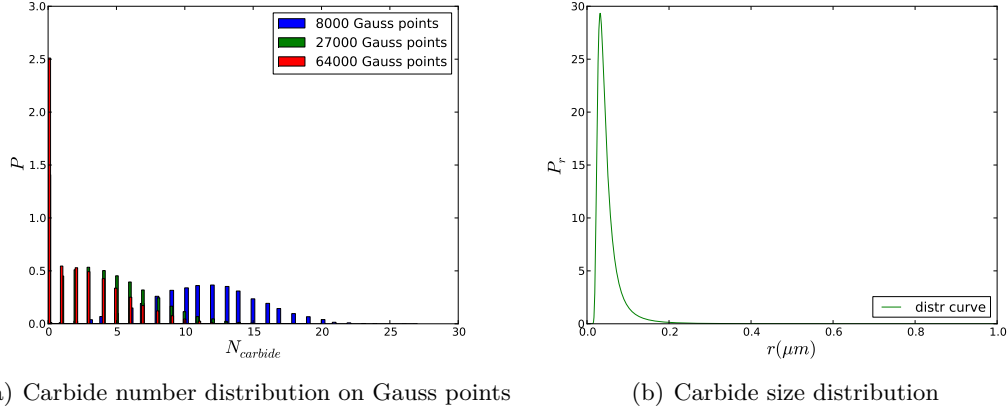
(a) Carbide number distribution on Gauss points

(b) Carbide size distribution

Figure 12: Distribution of carbides

(a) Largest carbide size
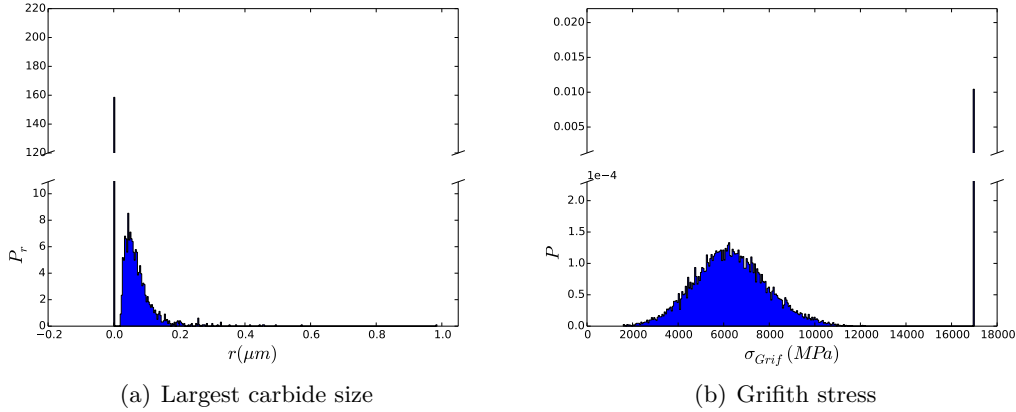
(b) Grifith stress

Figure 13: Distribution of the largest carbide size and the corresponding Grifith stress on each Gauss point

noted as σ^p. The maximal value of the local cleavage stress is then considered as the effective maximal stress at each gauss point.

$$\sigma_c^{max} = Max\{\sigma^p\} \tag{26}$$

This effective maximal cleavage stress is compared with the Griffith stress and the equivalent plastic deformation is compared with the critical value ε_p^{mini}. According to the model hypothesis **H6**, the fracture occurs as soon as the following criterion is verified:

$$\sigma_c^{max} \geq \sigma_{Grif}, \varepsilon_p^{equ} \geq \varepsilon_p^{mini} \tag{27}$$

In the finite element calculation, the simulation is performed step by step. Inside time steps all the variables are linearly interpolated.

The post treatment described above is repeated N_s times, for each realization the spatial arrangement of carbides is re-computed. In order to obtain the failure probability distribution

function, the whole results are sorted in increasing order of fracture time. A rank i=1,2... N_s is allocated to each result and the corresponding fracture probability P_R is given as :

$$P_R = \frac{i - 0.5}{N_s} \tag{28}$$

Equation 24 is employed to simulate the distribution of carbides in both ferritic and bainitic phases. It should be noted that this is an approximation and that additional calculations can be carried out once the realistic distributions are obtained in each phase and eventually within the phases.

4.2   Results and discussion

The first calculation of cumulated failure probability has been carried out directly on the Voronoï aggregates. A result summary is provided in table 7 and the crack initiating locations (elements) are shown in figure 14, as well as the grain boundaries. The simulated failure curve at -150 °C and the separated responses of the two phases are shown in figure 15.

A conclusion can be drawn here that given the mechanism and hypothesis explicated above, while the crack initiation takes place only in ferrite at -196 °C, it occurs in both phases at -150 °C, especially at grain boundaries and model interfaces. This result is in accordance with anticipation, as in comparison to -150 °C, the σ_{Grif} is smaller at -196 °C, due to the smaller value of γ_p. In addition, softer ferritic grains are prone to higher strain levels thus are more likely to pass the threshold of plastic deformation compared to bainitic grains. For each calculation, the last criterion to be reached (Griffith stress or plastic strain) is denoted as critial. For each temperature, this critical criterion is reported in Table 7. At the lowest temperture of -196 °C, the plastic deformation is more critical than the cleavage stress, and the trend is opposite at -150 °C.

	Failure initiation		Critical : σ_{Grif}		Critical : ε_p^{mini}	
Temperature	-196 °C	-150 °C	-196 °C	-150 °C	-196 °C	-150 °C
Whole model	200	200	81	120	119	80
Ferrite	200	39	81	39	119	0
Bainite	0	161	0	81	0	80

Table 7: Failure calculation information at -150 °C and -196 °C for dual-phase Voronoï model

The initiating elements for the 200 carbide samplings are shown in Figure 14, together with the ferrite-bainite interfaces. Initiation sites are often close to these interfaces, also correlated with stress concentrations.

Figure 15 shows, for the dual phase calculation at -150 °C, the repartition of failure initiation site between the two phases. About 80% of initiation events occur in bainitic phase, which is consistent with the Griffith stress limiting failure mechanism as reported in Table 7

Figure 16 shows that while the principal stresses at 50% failure possibility for single-phase and dual-phase models are equal, the failure probability distribution significantly differs in the low probability regime for the two models. The failure curve of dual-phase model spreads broader than the single-phase one, indicating a lower Beremin exponent. This is rather
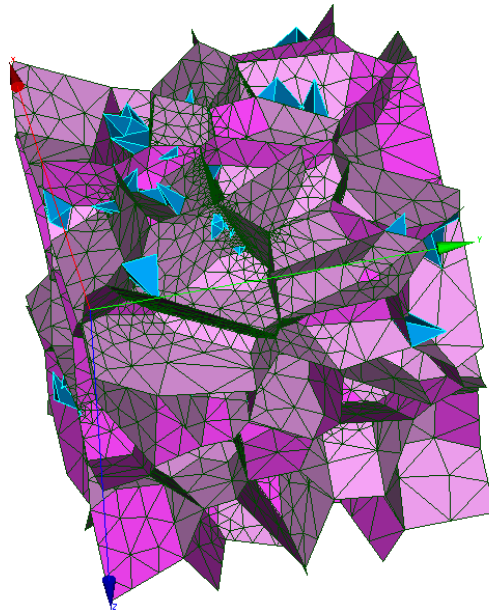
Figure 14: Distribution of crack initiating elements (in blue) at -150 °Cfor the dual-phase model. The ferrite-bainite interface mesh is displayed in magenta.

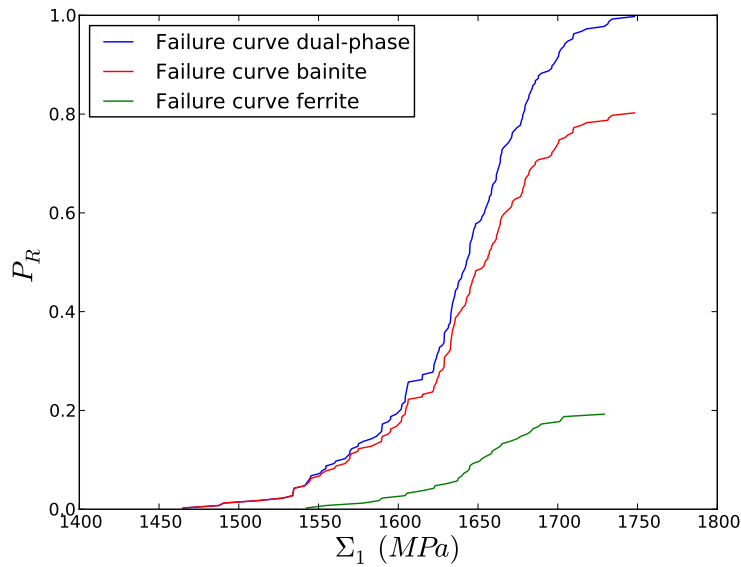Figure 15: Failure curve calculated at -150 °C

expected since increasing the microstructural and mechanical heterogeneties likely increases failure probability when considering a weakest link scenario. Naturally, this conclusion could be different depending on the considered carbide spatial distribution.

Figure 17 shows the cloud of carbide size and principal stress as crack initiates. It can be concluded that while relatively smaller ($0.6\mu m$ to $0.8\mu m$) carbides can lead to failure at high

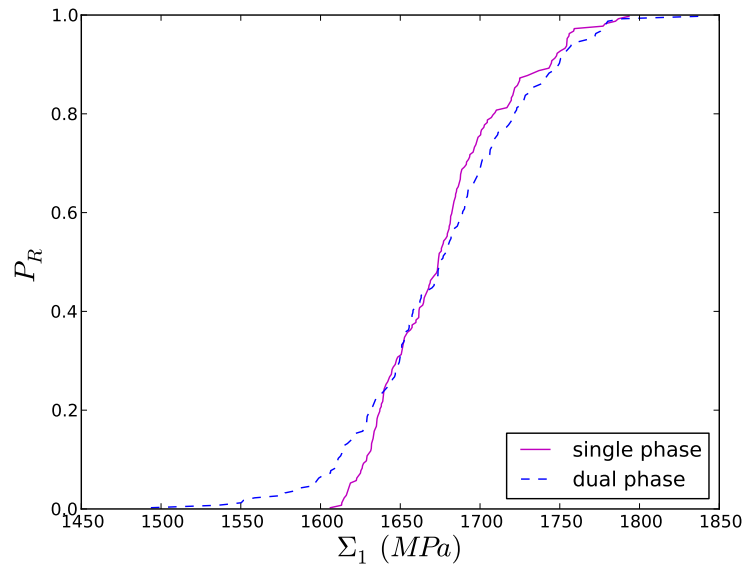Figure 16: Failure curves of single-phase and dual-phase models at -150 °C
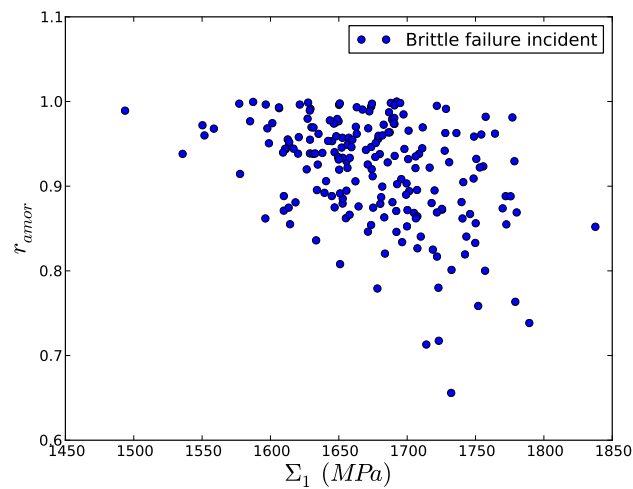

Figure 17: Carbide size at crack initiation against principal stress

principal stress, they do not seem critical when the macroscopic stress is low.

Conclusion

In conclusion, a preliminary step of this work consisted in identifying plastic flow models of the RPV steels, for two distinct micromechanical models : one single phase, and one dual phase. This identification, especially in the dual-phase case, could be improved by considering more information about phase-to-phase heterogeneities like initial dislocation densities. Other

improvement possibility would be to take advantage from in-situ SEM experiments together with digital image correlation to identify the mechanical contrast between the two phases.

Introducing the dual phase model was motivated by the phase distribution variation through the thickness. Coupling accurate microstructural description with plastic flow model and failure model would address the need of fracture toughness prediction at different depths of the component. Although these large scale heterogeneities were not yet predicted in this work, some preliminary assessments have indicated the interest of a dual phase model. Indeed, the dual phase model is associated with a lower macroscopic stress for lower failure probabilities.

This work also intends to illustrate the variety of computational micromechancals tools available that might help to understand or identify some root causes of failure, experimentally difficult or impossible to obtain. Naturally, the relevance of the obtained results strongly depends of the modeling hypothesis and the accuracy of mechanical fields computed at the microstructural scale. This in turn motivates the development of additional and complementary validation procedures for the different elementary bricks used in this approach : metallurgical quantitative information, plastic flow behaviour, failure behaviour.

References

[1] K. Wallin. Structural integrity assessment aspects of the master curve methodology. *Engineering Fracture Mechanics*, 77(2):285–292, January 2010. ISSN 0013-7944.

[2] B.-S Lee, J.-H Hong, W.-J Yang, M.-Y Huh, and S.-H Chi. Master curve characterization of the fracture toughness in unirradiated and irradiated RPV steels using full- and 1/3-size pre-cracked charpy specimens. *International Journal of Pressure Vessels and Piping*, 77(10):599–604, August 2000. ISSN 0308-0161.

[3] J Bohmert, H.-W Viehrig, and A Ulbricht. Correlation between irradiation-induced changes of microstructural parameters and mechanical properties of RPV steels. *Journal of Nuclear Materials*, 334(1):71–78, August 2004. ISSN 0022-3115.

[4] R. Kempf, H. Troiani, and A. M. Fortis. Effect of lead factors on the embrittlement of RPV SA-508 cl 3 steel. *Journal of Nuclear Materials*, 434(1?3):411–416, March 2013. ISSN 0022-3115.

[5] Z. Lu, R.G. Faulkner, and P.E.J. Flewitt. The role of irradiation-induced phosphorus segregation in the ductile-to-brittle transition temperature in ferritic steels. *Materials Science and Engineering: A*, 437(2):306–312, November 2006. ISSN 0921-5093.

[6] M. Valo, L. Debarberis, A. Kryukov, and A. Chernobaeva. Copper and phosphorus effect on residual embrittlement of irradiated model alloys and RPV steels after annealing. *International Journal of Pressure Vessels and Piping*, 85(8):575–579, August 2008. ISSN 0308-0161.

[7] J.-P. Massoud, S. Bugat, B. Marini, D. Lidbury, and S. V. Dyck. PERFECT : prediction of irradiation damage effects on reactor components: A summary. *Journal of Nuclear Materials*, 406(1):2–6, November 2010. ISSN 0022-3115.

[8] S. Leclercq, D. Lidbury, S. V. Dyck, D. Moinereau, A. Alamo, and A. Al Mazouzi. Perform 60 - prediction of the effects of radiation for reactor pressurevessel and in-core materials using multi-scale modelling - 60 years foreseen plant lifetime. *Journal of Nuclear Materials*, 406(1):193–203, November 2010. ISSN 0022-3115.

[9] F. Roters, P. Eisenlohr, L. Hantcherli, D.D. Tjahjanto, T.R. Bieler, and D. Raabe. Overview of constitutive laws, kinematics, homogenization and multiscale methods in crystal plasticity finite-element modeling: Theory, experiments, applications. *Acta Materialia*, 58(4):1152–1211, February 2010. ISSN 1359-6454.

[10] G. Monnet, C. Domain, S. Queyreau, S. Naamane, and B. Devincre. Atomic and dislocation dynamics simulations of plastic deformation in reactor pressure vessel steel. *Journal of Nuclear Materials*, 394(2-3):174–181, November 2009. ISSN 0022-3115.

[11] S. Queyreau, G. Monnet, and B. Devincre. Orowan strengthening and forest hardening superposition examined by dislocation dynamics simulations. *Acta Materialia*, 58(17): 5586–5595, October 2010. ISSN 1359-6454.

[12] G. Monnet, S. Naamane, and B. Devincre. Orowan strengthening at low temperatures in bcc materials studied by dislocation dynamics simulations. *Acta Materialia*, 59(2): 451–461, January 2011. ISSN 1359-6454.

[13] G. Monnet, L. Vincent, and B. Devincre. Dislocation-dynamics based crystal plasticity law for the low- and high-temperature deformation regimes of bcc crystal. *Acta Materialia*, 61(16):6178–6190, September 2013. ISSN 1359-6454.

[14] F. Beremin, A. Pineau, F. Mudry, J.-C. Devaux, Y. D'Escatha, and P. Ledermann. A local criterion for cleavage fracture of a nuclear pressure vessel steel. *Metallurgical and Materials Transactions A*, 14(11):2277–2287, 1983-11-01. ISSN 1073-5623.

[15] J.-P. Mathieu, K. Inal, S. Berveiller, and O. Diard. A micromechanical interpretation of the temperature dependence of beremin model parameters for french RPV steel. *Journal of Nuclear Materials*, 406(1):97–112, November 2010. ISSN 0022-3115. doi: 10.1016/j. jnucmat.2010.02.025.

[16] M. Libert, C. Rey, L. Vincent, and B. Marini. Temperature dependant polycrystal model application to bainitic steel behavior under tri-axial loading in the ductile-brittle transition. *International Journal of Solids and Structures*, 48(14-15):2196–2208, July 2011. ISSN 0020-7683. doi: 10.1016/j.ijsolstr.2011.03.026.

[17] L. Vincent, L. Gelebart, R. Dakhlaoui, and B. Marini. Stress localization in bcc polycrystals and its implications on the probability of brittle fracture. *Materials Science and Engineering: A*, 528(18):5861–5870, July 2011. ISSN 0921-5093. doi: 10.1016/j.msea.2011.04.003.

[18] H. Altendorf, F. Latourte, D. Jeulin, M. Faessel, and L. Saintoyant. 3D reconstruction of a multiscale microstructure by anisotropic tessellation models. *Image Analysis & Stereology; Vol 33, No 2 (2014)*, pages –, 2014.

[19] N. Osipov, A. F. Gourgues-Lorenzon, B. Marini, V. Mounoury, F. Nguyen, and G. Cailletaud. Fe modelling of bainitic steels using crystal plasticity. *Philosophical Magazine*, 88(30-32):3757–3777, 2008.

[20] C.N. NGuyen, F. Barbe, N. Osipov, G. Cailletaud, B. Marini, and C. Petry. Micromechanical local approach to brittle failure in bainite high resolution polycrystals: A short presentation. *Computational Materials Science*, 64(0):62–65, November 2012. ISSN 0927-0256.

[21] B. Diawara. *Caracterisation quantitative de la microstructure de l'acier 16MND5 des cuves de REP*. PhD thesis, Universite de Grenoble, 2011.

[22] H. Bhadeshia. *Bainite in Steels - 2nd Edition*. Institute Of Materials Communications Ltd, 2001.

[23] S. Naamane. *Etude de la déformation plastique de la ferrite à basse température : simulation de dynamique des dislocations*. PhD thesis, Université Pierre et Marie Curie, 2008.

[24] M. Bethmont. Evolution de la ténacité dans l'épaisseur des viroles de cuves des réacteurs à eau préssurisée, EDF R&D internal report H-T40-1988-02586-FR, Oct. 1988.

[25] S. Renevey. *Approches globale et locale de la rupture dans le domaine de la transition fragile-ductile d'un acier faiblement allié*. PhD thesis, Paris XI Orsay, 1997.

[26] P. Hausild. *Transition ductile-fragile dans un acier faiblement allié*. PhD thesis, École Centrale Paris, 2002.

[27] Jean-Philippe Mathieu. *Analyse et modélisation micromécanique du comportement et de la rupture fragile de l'acier 16MND5 : prise en compte des hétérogénéités microstructurales*. PhD thesis, Ecole Nationale Supérieure d'Arts et Métiers, 2006.

[28] A. Rossol. *Détermination de la ténacité d?un acier faiblement allié à partir de l"essai Charpy instrumenté*. PhD thesis, Ecole Centrale Paris, 1998.

[29] E. Rauch. *Etude de l'écrouissage des métaux - Aspects microstructuraux et lois de comportement*. PhD thesis, Institut National Polytechnique de Grenoble, 1993.

[30] S. Naamane, G. Monnet, and B. Devincre. Low temperature deformation in iron studied with dislocation dynamics simulations. *International Journal of Plasticity*, 26(1):84–92, January 2010. ISSN 0749-6419.

[31] S. Queyreau, G. Monnet, and B. Devincre. Slip systems interactions in α-iron determined by dislocation dynamics simulations. *International Journal of Plasticity*, 25(2):361–377, February 2009. ISSN 0749-6419.

[32] M. Berveiller and A. Zaoui. An extension of the self-consistent scheme to plastically-flowing polycrystals. *Journal of the Mechanics and Physics of Solids*, 26(5–6):325–344, October 1978. ISSN 0022-5096.

[33] E. Kröner. Zur plastischen verformung des vielkristalls. *Acta Metallurgica*, 9(2):155 – 161, 1961. ISSN 0001-6160.

[34] F. Barbe, S. Forest, and G. Cailletaud. Intergranular and intragranular behavior of polycrystalline aggregates.part 2: Results. *International Journal of Plasticity*, 17(4): 537–563, 2001. ISSN 0749-6419.

[35] J.P Cottu, J.P Peyrade, P Chomel, and P Groh. Etude en traction de l'adoucissement du fer de haute pureté par le carbone à basse temperature. *Acta Metallurgica*, 26(8): 1179 – 1188, 1978. ISSN 0001-6160.

[36] H. Lim, M.G. Lee, J.H. Kim, B.L. Adams, and R.H. Wagoner. Simulation of polycrystal deformation with grain and grain boundary effects. *International Journal of Plasticity*, 27(9):1328 – 1354, 2011. ISSN 0749-6419.

[37] K. Wallin, T. Saario, and K. Trrnen. Statistical model for carbide induced brittle fracture in steel. *Metal Science*, 18(1):13–16, 1984-01-01T00:00:00.

[38] B. Tanguy, C. Bouchet, S. Bugat, and J. Besson. Local approach to fracture based prediction of the delta-T56J and deltatK1c100 shifts due to irradiation for an A508 pressure vessel steel. *Engineering Fracture Mechanics*, 73(2):191–206, January 2006. ISSN 0013-7944.

[39] B. Tanguy. *Modélisation de l'essai Charpy par l'approche locale de la rupture. Application au cas de l'acier 16MND5 dans le domaine de transition.* 2001.

[40] S. Ortner, J. Duff, and D.W. Beardsmore. Characterisation of Euro-A reference steel for application of a model of brittle fracture. Technical report, EIG/15234/R003-Project PERFECT, SERCO Assurance, 2005.

[41] M.H. MacDougall. *Simulating Computer Systems.* M.I.T. Press, Cambridge MA, 1987.